



This is a repository copy of *Hydrogen suppression of dislocation cell formation in micro and nano indentation of pure iron single crystals*.

White Rose Research Online URL for this paper:  
<https://eprints.whiterose.ac.uk/170061/>

Version: Accepted Version

---

**Article:**

Gong, P., Katzarov, I., Nutter, J. et al. (3 more authors) (2021) Hydrogen suppression of dislocation cell formation in micro and nano indentation of pure iron single crystals. *Scripta Materialia*, 194. 113683. ISSN 1359-6462

<https://doi.org/10.1016/j.scriptamat.2020.113683>

---

Article available under the terms of the CC-BY-NC-ND licence  
(<https://creativecommons.org/licenses/by-nc-nd/4.0/>).

**Reuse**

This article is distributed under the terms of the Creative Commons Attribution-NonCommercial-NoDerivs (CC BY-NC-ND) licence. This licence only allows you to download this work and share it with others as long as you credit the authors, but you can't change the article in any way or use it commercially. More information and the full terms of the licence here: <https://creativecommons.org/licenses/>

**Takedown**

If you consider content in White Rose Research Online to be in breach of UK law, please notify us by emailing [eprints@whiterose.ac.uk](mailto:eprints@whiterose.ac.uk) including the URL of the record and the reason for the withdrawal request.



[eprints@whiterose.ac.uk](mailto:eprints@whiterose.ac.uk)  
<https://eprints.whiterose.ac.uk/>

# Hydrogen suppression of dislocation cell formation in micro and nano indentation of pure iron single crystals

Peng Gong<sup>1</sup>, Ivaylo Katzarov<sup>2,3</sup>, John Nutter<sup>1</sup>, Anthony T. Paxton<sup>2</sup>, Bradley Wynne<sup>1</sup>, W. Mark Rainforth<sup>1</sup>

1. Department of Materials Science and Engineering, University of Sheffield, Mappin Street, Sheffield, S1 3JD, UK.
2. Department of Physics, King's College London, Strand, London, WC2R 2LS, UK.
3. Bulgarian Academy of Sciences, Institute of Metal Science, 67, Shipchenski prohod Str., 1574, Sofia, Bulgaria

## Abstract

The influence of hydrogen on dislocation mobility in pure single crystal iron subjected to micro- and nanoindentation testing perpendicular to the (100) plane has been analysed using electron back-scattered diffraction (EBSD) and transmission electron microscopy (TEM) and simulated using the self-consistent kinetic Monte-Carlo (SCKMC) method. The nanoindentation load curve for the hydrogen free sample has two major constant load pop-ins, and multiple smaller pop-ins, whereas the hydrogen charged material has only one pop-in but with a longer loading release. A well defined cell structure was observed below the indenter in the hydrogen free condition, but the dislocations were homogeneously distributed in the hydrogen charged sample. The SCKMC simulations showed that it is difficult for dislocations to glide out of the primary slip plane after hydrogen charging compared with the hydrogen free sample under the present loading conditions.

**Keywords:** Pure iron single crystal; hydrogen induced softening; micro- and nanoindentation; self-consistent kinetic Monte-Carlo (SCKMC) simulations.

Hydrogen embrittlement has been studied for more than three decades but there are still many contradictory reports on the underlying mechanisms for embrittlement [1-3]. One explanation for this is that there are several mechanisms of hydrogen embrittlement occurring concurrently.

There are many embrittling mechanisms proposed of which three are widely reported: (1) stress-induced hydride formation and cleavage [4-7]; (2) hydrogen enhanced localized plasticity (HELP) [8-12], which depends on the dislocation mobility increasing owing to a reduction in activation energy of dislocation motion with hydrogen atoms in their core. The fracture process is a highly localized plastic failure process rather than an embrittlement; and (3) hydrogen induced decohesion (HEDE) [13, 14]. This mechanism assumes that the atomic bonding at the crack tip is weakened by the presence of hydrogen in solid solution. Many experimental studies have been reported on hydrogen embrittlement related mainly to these three mechanisms, mostly focussing on mechanical properties and microstructures after tensile or fatigue testing to failure [15-17].

Fundamental to the embrittling mechanisms is an understanding of the effect of hydrogen on the dislocation mobility and whether it promotes hardening or softening. Much work has been undertaken by Kimura, Matsui and co-workers [18-21], who showed that hydrogen can induce softening in very high purity iron single crystals in the temperature range 200-273K, but hardening occurs in conventional purity single crystal iron at room temperature or at temperatures below 200K. However, the influence of hydrogen on dislocation nucleation and mobility at the onset of deformation is much less studied and it is still an open question to how hydrogen hardens or softens alloys [22–28]. Thus, to answer these questions and avoid these complications, a high purity iron single crystal with the (100) plane parallel to the indentation surface was chosen. Micro and nanoindentation was undertaken on the hydrogen free and hydrogen charged conditions to observe the effect of hydrogen on the dislocation nucleation and mobility with the onset deformation.

Iron single crystals, with a (100) orientation, were purchased from Goodfellow, Cambridge, UK with a purity of 99.98%, with a sample size of  $\phi 10\text{mm} \times 2\text{mm}$ . The (100) orientation was

selected as it gives 4 symmetrical slip systems, which simplifies the modelling. The single crystal also avoids the effects of grain boundaries etc. The carbon content of the single crystal was measured at 200ppm. Specimens with the original size were prepared by standard metallographic methods on the surface for micro- and nanoindentation tests, which included grinding from P400 to P1200 and polishing up to 0.04  $\mu\text{m}$  colloidal silica particles. To remove the grinding and polishing induced surface stress the specimens were electropolished with an electrolyte solution of 5% perchloric acid, 35% butoxyethanol and 60% methanol. For hydrogen charged specimens electrochemical hydrogen charging was undertaken using 1 g/L in an aqueous solution of 3 wt% NaCl and 0.3 wt%  $\text{NH}_4\text{SCN}$  with a current density of 10  $\text{mA cm}^2$  for 24 hours at room temperature. This led to a hydrogen concentration in the sample of  $30 \pm 3$  appm as measured by thermal desorption spectroscopy.

Microindentation testing was performed using a Micro Materials Nano Test Vantage with the indentation axis parallel to the test sample's surface (i.e., (100) plane). The opposing surface to the test surface was ground flat and parallel. Specimens were mounted to a precision ground hardened steel plate with a thin layer of adhesive. Indentation tests were run with a constant crosshead speed of 0.1 mm/min with incremental unloading (50–30 % of the peak force) and reloading cycles until the specified 40 cycles was reached. A total of 17 tests were performed. A spherical tungsten-carbide tip was used for all tests with a radius of 19  $\mu\text{m}$ . The standard method for converting indentation load-displacement data into indentation stress-strain curves was followed [29, 30]. Nanoindentation tests were carried out using a Bruker Hysitron TI Premier equipped with the continuous stiffness measurement with a 1  $\mu\text{m}$  radius spherical diamond tip. The tests were carried out under load control to peak displacements of 80 nm in all samples. The indentation strain rate was  $0.013\text{s}^{-1}$ . A total of 17 tests were performed for each condition.

The microindentation load displacement curve and its corresponding indentation strain-stress curves from hydrogen-free and hydrogen charged single crystals are shown in Figs. 1 (a) and (b). The indentation strain-stress curve for the hydrogen free sample can be divided into various stages: following yield, there is a region of rapid work hardening. The rate of work hardening gradually decreases to the end of the test. The stress strain curve for the charged sample is quite different. After the same elastic behaviour as the uncharged sample, the stress strain curve remains approximately linear to the end of the test, with no evidence of the rapid work hardening observed in the hydrogen free sample. The indentation stress of the charged and uncharged converges towards the end of the test. Clearly, the hydrogen significantly affected the work hardening behaviour.

In order to accurately measure the effect of hydrogen on dislocation structure and mobility, nanoindentation tests with a loading force up to 1000  $\mu\text{N}$  was used on the hydrogen free and hydrogen charged single crystals. The nanoindentation loading displacement curves show four stages: initial elastic loading; an excursion in depth (pop-in), which is associated with the onset of plasticity; subsequent plastic loading; and elastic unloading in Fig. 1 (c). In the hydrogen free samples, multiple pop-in events are observed for most of the tests, with the first two being distinct while others at higher loads were only just above the noise level. The second pop-in was 150-200 $\mu\text{N}$  higher than the first, with a similar increase in indentation depth for each pop-in. In contrast, a single pop-in event was observed in the hydrogen charged condition. In this first pop-in, a distinctly longer release stage is observed compared with the hydrogen free sample.

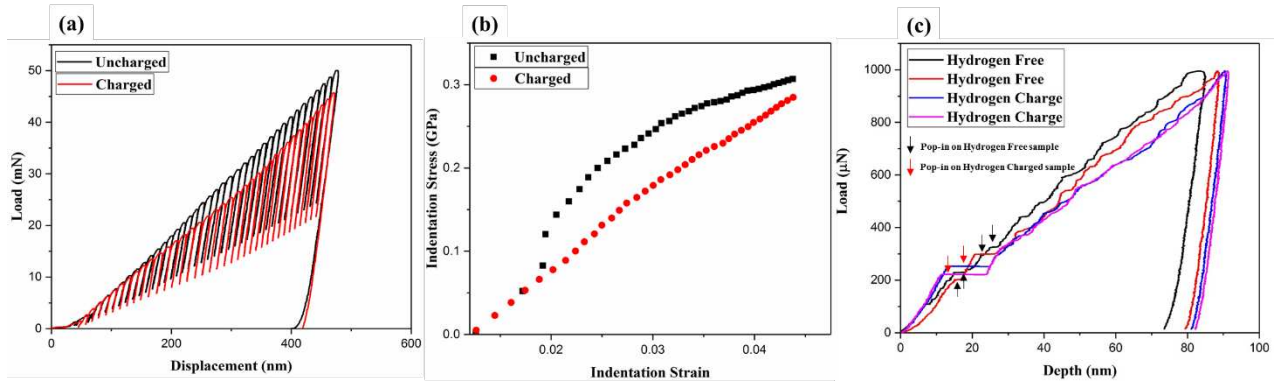


Fig. 1 (a) Microindentation load-displacement curve; (b) the microindentation stress-strain curve calculated from the microindentation load-displacement curve; and (c) nanoindentation load-displacement curve, on hydrogen-free and hydrogen charged pure iron single crystal.

In order to observe the dislocation substructure, TEM specimens were extracted from the site-specific locations of the indenter surface using the FIB lift-out technique with a FEI Helios Nanolab 650 SEM/FIB. Three indents were examined per condition. During the FIB lift-out from the indenter surface, platinum (Pt) was slowly deposited on the location of interest to preserve the corresponding indentation surface at the location. TEM observations of the FIB samples were then conducted in a JEOL F200 TEM operated at an accelerating voltage of 200 kV. Orientation mapping was undertaken in the TEM using a Nanomegas ASTAR system, an automated crystal orientation and grain boundaries mapping tool using precession electron diffraction. Diffraction patterns were recorded using the external camera, with an exposure time of 40 ms.

The TEM results were found to be very similar for each of the three indents examined. The results of crystal orientation and grain boundary mapping are given in Fig. 2. In the hydrogen-free condition, the band contrast (BC) image in Fig. 2 (a) shows the heterogeneous distribution of dislocations, and the KAM image in Fig. 2 (b) shows that there are dislocation cell structures under the indenter. In contrast, in the hydrogen-charged condition, the band contrast image in Fig. 2 (c) shows a more homogeneous dislocation distribution than the uncharged condition, while the KAM image shown in Fig. 2 (d) further demonstrates that there are no obvious

dislocation cell structures. Thus, there was no obvious evidence of dislocation recovery microstructures. This is consistent with the absence of additional pop-in events in the nanoindentations curves and also consistent with the absence of hardening in the microindentation curves.

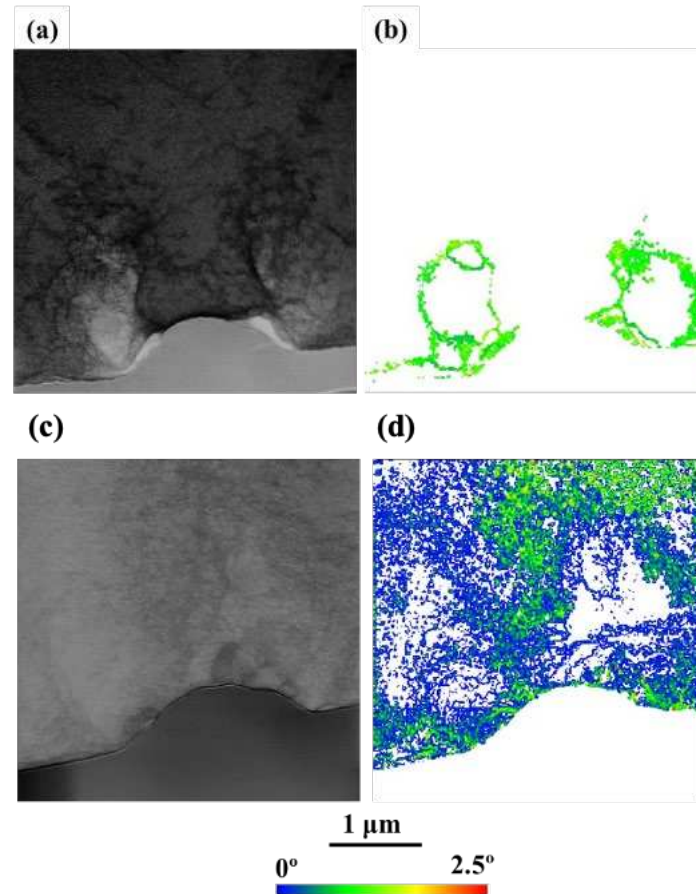


Fig. 2 Orientation maps on the cross section nanoindentation FIB TEM lift out samples with hydrogen free (a,b) and hydrogen charged (c,d) ((a) and (c) band contrast images; (b) and (d) KAM images).

To observe the details of dislocation structures, STEM bright field (BF) and high angle annular dark field (HAADF) results are shown in Fig. 3. Lower magnification was used to observe the whole area underneath the nanoindenter in the hydrogen-free sample, which shows the high density of the dislocations on both sides of the indenter, but under the indenter, the dislocation density is much lower than the edge of the indenter. In the hydrogen charged sample under the same imaging conditions, the dislocation structures were homogeneously distributed with no

significant difference in dislocation density at the sides or below the indenter. Moreover, the dislocation density in the hydrogen charged sample is less than the hydrogen free sample. With increased magnification to observe at one side of the indenter (left-hand side as the image is viewed) for both the hydrogen free and hydrogen charged samples, difference in dislocation cell structures becomes much more obvious. The hydrogen-free sample exhibits clear dislocation tangles/ cell walls, which are largely absent in the hydrogen charged sample.

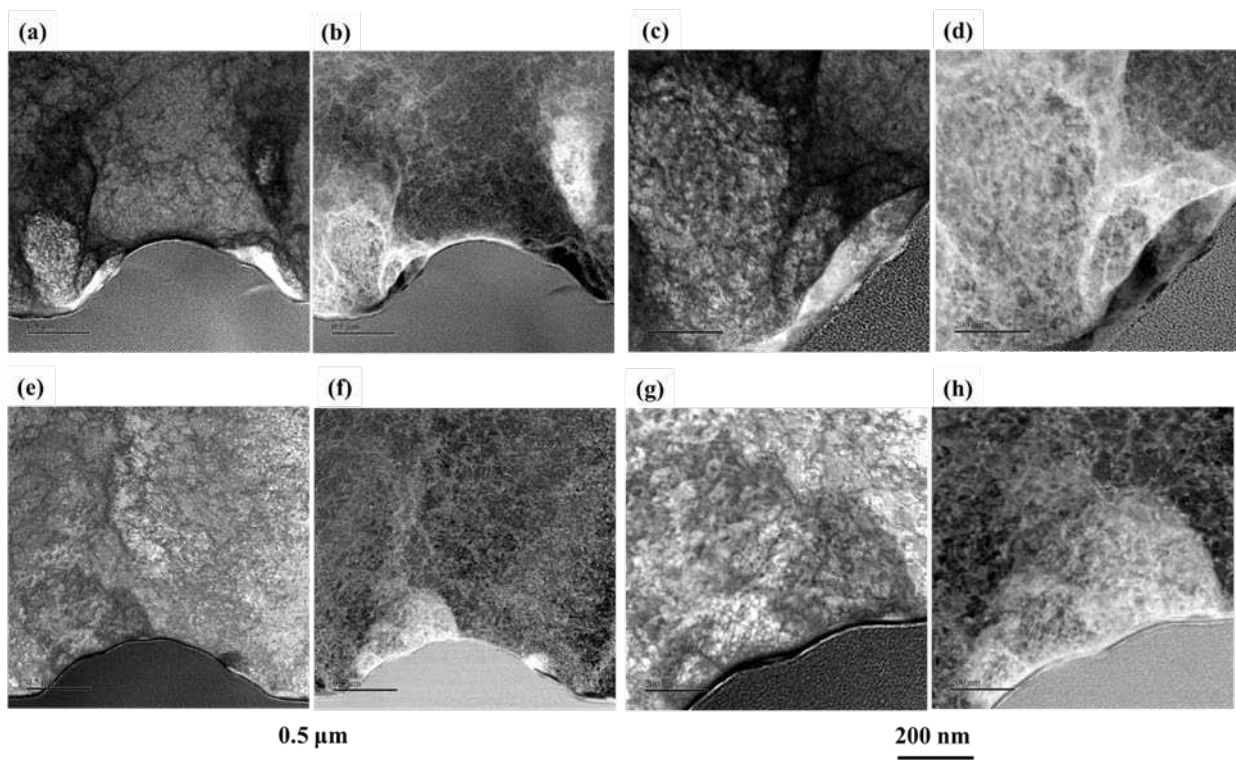


Fig. 3 STEM on the cross section nanoindentation FIB STEM lift out samples with hydrogen free (a-d) and hydrogen charge (e-h); (a) and (b) BF and DF STEM image with lower magnification on the cross section of nanoindentation; (c) and (d) BF and DF STEM image with higher magnification on the left hand side of cross section of nanoindentation; (e) and (f) BF and DF STEM image with lower magnification on the cross section of nanoindentation; (g) and (h) BF and DF STEM image with higher magnification on the left hand side of cross section of nanoindentation.

To further understand why hydrogen enhances the dislocation mobility but reduces the extent of formation of dislocation tangles or cell structures, modelling work was undertaken. The mobility of  $1/2$   $[111]$  screw dislocations in hydrogen charged and uncharged  $\alpha$ -Fe have been analysed through simulation of the specific mechanisms of motion of an individual dislocation.

We use self-consistent kinetic Monte-Carlo (SCKMC) simulations of  $1/2$  [111] screw dislocations and track their glide in order to obtain a realistic description of the dynamics of a dislocation line over long time scales [31, 32]. Specific features of the SCKMC model are: (i) simultaneous kink nucleation, migration and hydrogen jumping; (ii) kink pair formation energy depending on average dislocation velocity and hydrogen distribution and mobility within the core. We perform kMC simulations with computational time of 120 h to describe dislocation movement distance of 50 nm in H charged bcc Fe for a movement time  $3 \cdot 10^{-4}$  s. The strain change for the indentation experiments for this time interval is negligible - about  $4 \cdot 10^{-6}$ . However, due to the rapid H diffusion in bcc Fe the SKkMC model takes into account the effect of H migration on kink-pair formation enthalpy and kink propagation along the dislocation line. We simulate the competing effects of softening by enhanced kink-pair generation and hardening by solute pinning. Results from our simulations show that the behaviour of the screw dislocation depends significantly on the applied shear stress and hydrogen concentration in the bulk. The kink-pair nucleation rates in the three cross-slip (110) glide planes depend on the magnitude and the direction of the maximum resolved shear stress (MRSS). The results presented in this section are obtained for non-symmetrical triple slip conditions in which the MRSS plane bisects the primary glide plane at an angle of  $15^\circ$ . Our simulations indicate that the mobility of screw dislocations induced by this orientation of the MRSS plane approximately corresponds to the average dislocation mobility resulting from different shear stress orientations [31].

After the formation of a stable double kink the two kinks will separate in opposite directions. First of all, the angle describing the deviation of the dislocation from the primary slip plane at an applied stress  $\tau = 30$  MPa as a function of the average distance covered by the dislocation is shown in Fig. 4 (a) on both hydrogen free and hydrogen charged conditions. The results show that with a hydrogen free condition, the deviation angle remains constant with

increasing distance. However, for the hydrogen charged condition, the deviation angle rapidly reduces after the distance increases to  $30\text{\AA}$ . Secondly, for pure iron, we know that the secondary Peierls barrier is low and kink migration is not thermally activated. Thus, the kink migration speed is so fast that a kink pair has separated to the ends of the dislocation with a typical length of  $1000b$  before the next kink pair is activated [32]. Hence kink collision does not occur. The kink pair nucleation in the secondary (110) glide planes, with formation rate depending on the corresponding RSS, leads to cross-slip of the dislocation. After moving on a secondary plane, dislocation cross-slip occurs again, resuming gliding along the primary glide plane (Fig. 4 (b)). This zigzag motion of the dislocation leads on average to glide out of the primary slip plane. However, if a kink sweeps past a hydrogen atom trapped behind the dislocation line, then hydrogen ends up in a higher enthalpy trap site [33], which implies that thermal activation is then required for the kink to proceed. SCKMC simulations show that the dislocation mobility out of the primary slip plane decreases significantly for H concentration  $C_H = 30$  appm and applied shear stress  $\tau = 30$  MPa.

Fig. 4 (b,c) show simulations at a resolved shear stress,  $\tau = 30$  MPa, and  $T = 300$  K. In each panel the upper black line shows a snapshot of a moving  $1/2[111]$  screw dislocation projected onto the primary (110) glide plane, while the lower black line shows the same dislocation at the same time projected onto the perpendicular (112) plane. This second projection serves to indicate the extent to which the dislocation deviates from its primary glide plane into the two cross slip planes in the [111] zone. The red lines indicate debris (prismatic loops) left behind due to the creation of jogs and superjogs and subsequent unzipping. Due to the high H concentration in the dislocation core, the hydrogen trapping effect leads to a reduction of the average kink velocity and increasing probability for the collision of kinks propagating simultaneously in different planes and creation of self-pinning jogs. This is illustrated in Fig. 4 (c), which now shows significant deviation from a straight dislocation on the primary slip

plane and segments of trailing debris in the microstructure. The significant reduction of kink velocity along the secondary slip planes, resulting from the high H concentration and lower RSS, lead to a reduced dislocation glide out of the primary slip plane. The results from our simulations indicate that, at low stresses, the misorientation of the screw dislocation decreases with hydrogen charging condition, and the movement in the direction of the secondary glide plane is pretty well suppressed. It has been commonly accepted that a requirement for cell formation is that dislocations have sufficient mobility out of their slip plane. According to our model prediction, at low shear stresses the deviation from the primary slip plane in the presence of H is lower than the deviation in the uncharged Fe. Hence, the probability for formation of a cell structure in hydrogen free condition is expected to be higher than in hydrogen charged iron. At higher shear stresses (above 100 MPa) SChMC simulations [32] indicate that the misorientation of the screw dislocation increases with hydrogen charging condition. The experimental observations in these conditions also show the formation of dislocation cell structure in H charged Fe [34]. At high stresses the kink velocity is high even in the secondary glide planes, which, in combination with the higher probability for kink-pair formation in the secondary (110) planes, leads to enhanced deviation from the primary slip plane in presence of H than the deviation in the uncharged Fe. Therefore, the ease with which screw dislocations cross slip and glide out of the primary slip plane in H charged Fe depends on the combination of the applied shear stress and hydrogen concentration.

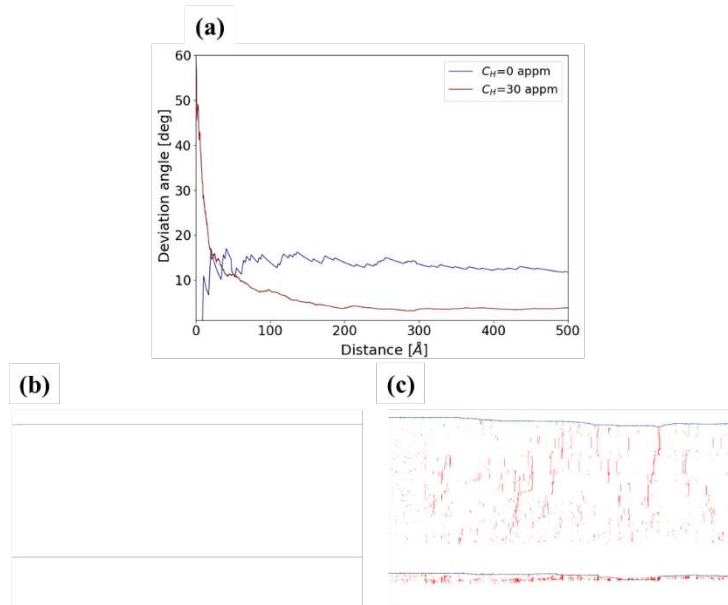


Fig. 4 (a) the angle describing the deviation of the dislocation from the primary slip plane as a function of the average distance covered by the dislocation.  $\sigma = 30$  MPa,  $T = 300$ K; (b), (c) The snapshots of a moving  $1/2$   $[111]$  screw dislocation (black line) projected onto (110) (upper line) and (112) (lower line) planes. The red lines indicate trailing debris. Blue dots represent the positions of hydrogen atoms.  $\tau = 30$  MPa,  $T = 300$ K: (b)  $C_H = 0$  and (c)  $C_H = 30$  appm.

These SCKMC simulations allow an understanding of the microindentation and nanoindentation curves and the resultant dislocation structures observed underneath the indents. A first pop-in event was observed in the nanoindentation curves for the hydrogen charged and hydrogen free samples, Fig. 1 (c). A pop-in is associated with a sudden increase in indentation depth under a constant load. The load for the first pop-in was similar for the charged and hydrogen free samples. It is widely accepted that the first pop-in is the result of the initiation of plastic deformation through dislocation slip. For a single crystal sample, there are a number of mechanisms that can produce pop-ins, as summarised by Pöhl [35]. Firstly, homogeneous dislocation nucleation is known to produce a pop-in event. This includes dislocation nucleation that is affected by interstitials. Similarly, unlocking and movement of pinned dislocations will produce a similar pop-in. The observation of the first pop-in at the same load for charged and uncharged samples suggests that hydrogen does not have any effect on the stress to nucleate and activate dislocation slip for a pure iron single crystal. However, the strain associated with

the pop-in was far larger for the hydrogen charged sample, compared to the hydrogen free material. The SCkMC simulations demonstrated that the presence of hydrogen significantly reduces dislocation glide out of the primary slip plane. Therefore, at low strains secondary slip is suppressed and therefore, in the absence of any other barriers in a single crystal, extensive glide on the primary slip plane occurs, leading to extended strain associated with the pop-in. In contrast, in the hydrogen free sample glide occurs out of the slip plane leading to dislocation tangles and a limit to the strain associated with the pop-in before work hardening resumes, as observed by TEM, Fig. 2.

The SCkMC simulations also explain the difference in work hardening behaviour observed in the microindentation, Fig. 1b, where the charged sample exhibited a lower work hardening rate. The suppression of glide out of the primary slip plane by the hydrogen is sufficient to reduce the extent of work hardening.

Beyond the initial pop-in, additional pop-in events are usually observed at higher loads, which are associated with further dislocation motion, dislocation multiplication, and the resultant evolution of complex dislocation structures [35]. The question then arises as to why the charged samples exhibit a single pop-in while the hydrogen free samples generally exhibit a second pop-in, which is the normal expected behaviour. There are two possibilities to explain this. Firstly, the absence of a second pop-in may simply be a result of the suppression of secondary slip by hydrogen. Such an explanation would be consistent with the observed dislocation structures and the microindentation work hardening curves. It is also consistent with the modelling presented here. Alternatively, the difference could be a result of the effect of hydrogen on the extent of the formation of Cottrell atmospheres from carbon at the dislocation core. The presence of hydrogen increases the dislocation velocity, but in a complex manner that depends strongly on the resolved shear stress and the hydrogen concentration [34]. If hydrogen charging increases the mobility of screw dislocations, then there is less chance of

Cottrell atmospheres forming and therefore less chance of a strain ageing effect. Moreover, in the present work, the single crystals had a high level of purity such that the formation of carbon induced atmospheres is unlikely. In addition, hydrogen charging did not alter the stress for the first pop in suggesting that Cottrell atmospheres had not formed on pre-existing dislocations. Thus, the formation of atmospheres was not believed to be responsible for the differences observed.

In conclusion, the microindentation stress strain curve for the uncharged sample shows the classical appearance with initially rapid work hardening, but with decreased hardening thereafter. In contrast, the hydrogen charged sample shows much lower rates of work hardening. The microstructural observations show that there were dislocation cell structures underneath the indenter in the hydrogen free condition. However, the same structures were not found in the hydrogen charged condition, rather a more homogenous distribution of dislocations is observed. These unusual experimental observations have been explained through self-consistent kinetic Monte-Carlo simulations which demonstrates that hydrogen suppresses the suppression of glide out of the primary slip plane.

#### Acknowledgements

We acknowledge the support of EPSRC under the Programme Grant HEmS, EP/L014742. I.H.K. acknowledges support from Bulgaria National Science Fund (BNSF) under Programme grant KP-06-H27/19.

#### References

- [1]. S. Lynch, *Corros. Rev.* 30(2012), 105-123.
- [2]. Y. Murakami, T. Kanezaki, Y. Mine, S. Matsuoka, *Metal. Mat. Trans.: A* 39(2008), 1327-1339.
- [3]. J. Song, W. Curtin, *Nature Mater.* 12(2013), 145-151.
- [4]. D.G. Westlake, *Trans. ASM* 62(1969), 1000.

- [5]. H.K. Birnbaum, M. Grossbeck, S. Gahr, *Hydrogen in Metals* (ASM, Ohio ed) by in I. M. Bernstein and A.W. Thompson, 1973, pp. 303.
- [6]. S. Gahr, M.L. Grossbeck, H. K. Birnbaum, *Acta Metall.* 25(1977), 125-134.
- [7]. D. Shih, I.M. Robertson, H. K. Birnbaum, *Acta Metall.* 36(1988), 111-124.
- [8]. C.D. Beachem, *Metall. Mater. Trans.: B* 3(1972), 441-455.
- [9]. H.K. Birnbaum, *Environment-Induced Cracking of Metals*, in: R. P. Gangloff and M. B. Ives (eds.), N.A.C.E., Houston, 1988, pp. 21.
- [10]. S.M. Meyers, M.I. Baskes, H.K. Birnbaum, J.W. Corbett, G.G. Deleo, S.K. Estricher, E.E. Haller, P. Jena, N.M. Johnson, R. Kircheim, S.J. Pearton, M.J. Stavola, *Rev. Mod. Phys.* 64(1992), 559.
- [11]. E. Sirois, P. Sofronis, H.K. Birnbaum, in: S. M. Bruemmer et al. (eds.), *Fundamental Aspects of Stress Corrosion Cracking*, The Minerals, Metals and Materials Society, New York, 1992, pp. 173.
- [12]. H.K. Birnbaum, in N. Moody and A. W. Thompson (eds.), *Hydrogen Effects on Materials Behaviour*; The Minerals, Metals and Materials Society, New York, 1990, pp. 639.
- [13]. E.A. Steigerwald, E.W. Schaller, A.R. Troiano, *Trans. Metall. Soc. AIME*, 218(1960), 832.
- [14]. R.A. Oriani, E.H. Josephic, *Acta Metall.* 22(1974), 1065-1074.
- [15]. M. Koyama, C.C. Tasan, E. Akiyama, K. Tsuzaki, D. Raabe, *Acta Metall.* 70(2014), 174-187.
- [16]. O. Barrera, D. Bombac, Y. Chen, *J. Mater. Sci.*, 53(2018), 6251-6290.
- [17]. N. Nanninga, A. Slifka, Y. Levy, C. White, *J. Res. Natl. Inst. Stand. Technol.* 115(2010), 437-452
- [18]. A. Kimura, H. Matsui, H. Kimura, *Mater. Sci. Eng.* 58 (1983), 211-222.

- [19]. H. Kimura, H. Matsui, *Scr. Metall.* 21(1987), 319-324.
- [20]. H. Matsui, H. Kimura, A. Kimura, *Mater. Sci. Eng.* 40(1979), 227-234.
- [21]. K. Oguri, H. Kimura, *Scr. Metall.* 14(1980), 1017-1022.
- [22]. Y. Takahashi, M. Tanaka, K. Higashida, H. Noguchi, *Scr. Mater.* 61(2009), 145-148.
- [23]. S. Wang, M.L. Martin, P. Sofronis, S. Ohnuki, N. Hashimoto, I.M. Robertson, *Acta Mater.* 69(2014), 275-282.
- [24]. M. Martin, P. Sofronis, I. Robertson, T. Awane, Y. Murakami, *Int. J. Fatigue* 57 (2013), 28-36.
- [25]. M.L. Martin, B.P. Somerday, R.O. Ritchie, P. Sofronis, I.M. Robertson, *Acta Mater.* 60(2012) 2739–2745.
- [26]. Y. Takahashi, J. Sakamoto, M. Tanaka, K. Higashida, H. Noguchi, *Scr. Mater.* 64(2011) 721-724.
- [27]. Y. Takahashi, M. Tanaka, K. Higashida, K. Yamaguchi, H. Noguchi, *Acta Mater.* 58, (2010) 1972-1981.
- [28]. J. Wang, S. Hata, Y.K. Takahashi, H. Sepehri-Amin, B.S.D.Ch.S. Varaprasad, T. Shiroyama, T. Schrefl, K. Hono, *Acta Mater.* 91(2015), 41-49.
- [29]. A. Khosravani, C. Ahmet, S.R. Kalidindi, *Acta Materialia* 123 (2017), 55-69.
- [30]. A. Khosravani, C.M. Caliendo, S.R. Kalidindi, *Metals* 10(2020), 18.
- [31]. M. Rhee, H.M. Zbib, J.P. Hirth, H. Huang, T.D.L. Rubia, *Modelling Simul. Mater. Sci. Eng.* 6(1998), 467-492.
- [32]. I.H. Katzarov, D.L. Pashov, A.T. Paxton, *Phys. Rev. Mater.* 1(2017), 033602-1-11.
- [33]. P. Gong, I.H. Katzarov, J. Nutter, A.T. Paxton, W.M. Rainforth, *Sci. Rep.* 10(2020), 10209-1-14.
- [34]. M. Itakura, H. Kaburaki, M. Yamaguchi, T. Okita, *Acta Mater.* 61(2013), 6857-6867.
- [35]. F. Pöhl, *Sci. Rep.* 9 (2019), 15350-1-12.

